CATAPULT

NOVEL CATALYST STRUCTURES EMPLOYING PT AT ULTRA LOW AND ZERO LOADINGS FOR AUTOMOTIVE MEAS

Grant agreement no.: 325268
***Start date**: 01.06.2013 – **Duration**: 36 months*
***Project Coordinator**: Deborah Jones – CNRS*

DELIVERABLE REPORT

D6.2 – KINETIC MODEL OF THE ORR UNDER REACTION CONDITIONS FORMULATED	
Due Date	31st May 2015
Author (s)	L. Sabo, D. Fantauzzi, T. Zhu, J. E. Mueller, T. Jacob
Workpackage	WP6 Modelling
Workpackage leader	Timo Jacob
Lead Beneficiary	UUlm
Date released by WP leader	16th September 2015
Date released by Coordinator	17th September 2015

DISSEMINATION LEVEL		
PU	*Public*	***X***
PP	*Restricted to other programme participants (including the Commission Services)*	
RE	*Restricted to a group specified by the consortium (including the Commission Services)*	
CO	*Confidential, only for members of the consortium (including the Commission Services)*	

NATURE OF THE DELIVERABLE		
R	*Report*	***X***
P	*Prototype*	
D	*Demonstrator*	
O	*Other*	

SUMMARY	
Keywords	*Pt(111), oxygen reduction reaction, kinetic model*
Abstract	*DFT calculations are used to identify possible ORR reaction mechanisms, allowing the construction of a simple kinetic model to gain qualitative information about contribution of the individual pathways to the overall ORR. Using the calculated activation barriers, a microkinetic model for the water formation in gas-phase is established and the influence of temperature and partial pressure of the reactants on the reaction rates and thus on the preferred mechanism, is investigated.*

REVISIONS

Version	Date	Changed by	Comments
0.1	08/06/2015	L. Sabo	Draft
0.2	15/09/2015	L. Sabo, T. Jacob	Incorporation of suggestions by DJ

FORMULATION OF KINETIC MODEL OF THE ORR UNDER REACTION CONDITIONS

Introduction

One of CATAPULT's modelling efforts is to understand the high catalytic ORR activity of extended Platinum surfaces. Though the overall aim is to reduce the amount of Pt, here we aim to first understand the reaction mechanism on Pt and to identify the most important reaction steps of the overall catalytic process. Based on this knowledge we will be able to propose ways to reduce the Pt-loading by preparing catalysts with an increased number of active sites, or even to suggest alternative catalysts with similar properties. In order to achieve this goal, here a multi-scale approach is used to investigate the ORR on well-defined single crystal Pt surfaces.

In former DFT studies, we investigated the mechanism of the ORR on Pt(111) under gas-phase conditions, under the influence of a solvent and under ambient conditions. For the coupled proton and electron transfer (CPET) we considered both Langmuir-Hinshelwood (LH) and Eley-Rideal (ER) type mechanisms (see Deliverable 6.1 for details), finding three different possible reaction pathways: the O_2 dissociation mechanism, the OOH dissociation mechanism and the HOOH dissociation mechanism [1-3].

Based on the knowledge obtained in these studies, the next step was to perform a kinetic analysis. As described in the original CATAPULT-proposal, in this deliverable we describe the results of our kinetic analysis of the electrochemical oxygen reduction reaction on Pt electrodes. Further, we describe the generation of a corresponding microkinetic model to analyse the kinetic dynamics of the water formation reaction. In a first step this approach is then applied to study the gas-phase water formation process on Pt(111), which allowed for a direct comparison to literature data.

Rate constants under electrochemical conditions

Methodology

Based on former DFT calculations of the ORR on Pt(111) using a Pt_{35} cluster and the Jaguar program with B3LYP functional and LACVP** basis set, we use a simple model to calculate the potential dependent rate constants for the different ORR mechanisms. We assume that the potential dependence across the double layer is not linear, but follows Eyring's canonical transition state theory [4] and the rate constant $k(U)$ takes form of:

$$k(U) = \frac{k_B T}{h} \exp\left(\frac{-\Delta^{\ddagger} G_T(U)}{k_B T}\right) \quad (1)$$

where k_B is Boltzmann's constant, h is Planck's constant, T is temperature and $\Delta G_T(U)$ is the potential dependent barrier for the individual process. The CPET reaction is assumed to be a multistep process, where individual hydrogen atoms transfer from the bulk electrolyte to the electrode. However, the hydrogen barriers are not modelled dynamically as suggested by Marx [5], but for simplicity, only the relative energies between the initial and final state are changed in each CPET mechanism. For a steady-state concentration of unity for each intermediate, the slowest process for each mechanism is the one with the lowest rate constant.

Results

The rate constants are calculated for three ingoing processes, leading to dissociation of O^*–O^* (k_{O2}), O^*–OH^* (k_{OOH}) , HO^*–OH^* (k_{HOOH}) and two outgoing processes, leading to water formation H_2O^* (k_{out}) and the desorption of H_2O_2 ($k_{H2O2,off}$). As shown in figure 1, H_2O_2 can easily be formed at potentials lower than 0.4 V ($k_{HOOH} > k_{OOH} > k_{O2}$) and the bottleneck for the HOOH mechanism is either the HO–OH bond dissociation itself (k_{HOOH}) or the desorption of H_2O_2 from the surface ($k_{H2O2,off}$). In this potential range both processes of the H_2O_2 mechanism are considerably faster than the bottleneck processes in the OOH or O_2 mechanism, that is the O–OH respectively the O–O dissociation. However, in the four-electron reduction process the bottleneck is the water formation ($k_{out} < k_{HOOH}$). This could be due to accumulation of intermediates such as OH^* or H_2O^* on the surface, leading to electrode poisoning and decreasing the overall ORR activity. The desorption of H_2O_2 into the electrolyte is also possible ($k_{H2O2,off} > k_{out}$), allowing two-electron reduction processes. Experimental evidence is provided by Marković *et al.* by measuring a lower ORR activity at low potentials than at higher ones in rotating-disk experiments under acidic conditions [6] and observing both two- and four-electron processes at potentials 0.0-0.3 V [7].

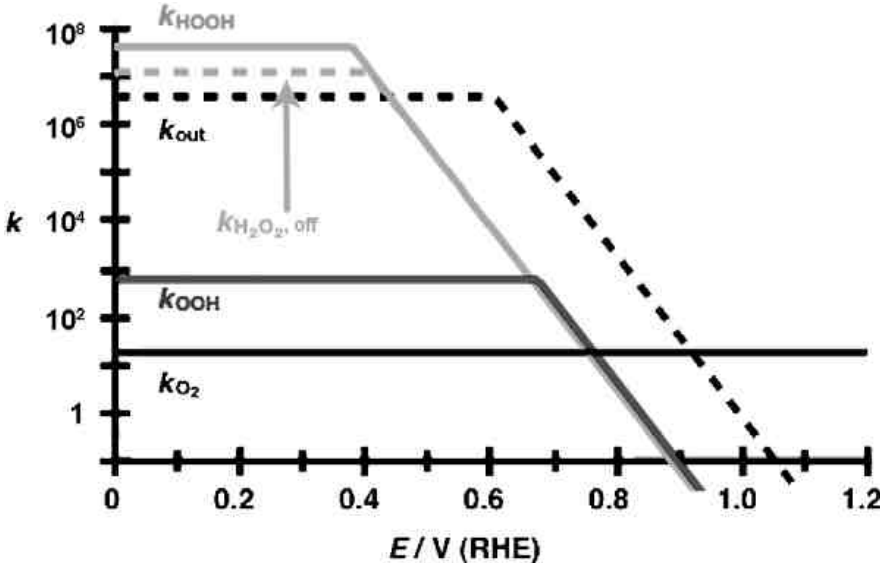

Figure 1: Calculated relative magnitude of the potential dependent rate constants for the different ORR mechanisms. Adsorption processes (ingoing) are shown as solid lines, whereas dashed lines represent the formation and desorption of products (outgoing). (Adapted from[2]).

As the rate constant for H_2O_2 formation decreases at potentials higher than 0.4 V, this process becomes now the bottleneck for the HOOH mechanism. Since both $H_2O_2^*$ and OOH^* formation have similar barriers in our calculation, we cannot determine which of both processes governs the ORR. At 0.43 V water formation becomes faster than any of the ingoing processes and as the hitherto rate determining H_2O_2 formation becomes slower with increased potential, we can conclude that now all three pathways contribute to the overall ORR activity.

At potentials above 0.6 V, the rate of water formation decreases and the formation of H_2O^* from OH^* is now the rate determining process. Above 0.65 V the rate of $H_2O_2^*$ formation has decreased to such an extent that the OOH pathway becomes more favourable. Thus OOH^* formation from O_2^* is now the rate determining step. Since the rate of this process also decreases with increasing potential, at 0.75 V a point is reached, where all three pathways contribute equally to the ORR activity in this model. As the O_2 dissociation process is completely potential independent in this model, this pathway becomes the most preferred for potentials above 0.75 V. However, above 0.95 V the rate of water formation has decreased so far, that this process becomes the bottleneck again (same as at potentials below 0.4 V). On a microscopic scale we can imagine the electrode becoming saturated with O^* and OH^*, causing the ORR to disrupt.

Microkinetic Modeling of the ORR in gas-phase

Methodology

The microkinetic simulations were performed using the MKM/CXX software developed by the Inorganic Materials Chemistry group at the Eindhoven University of Technology [8]. The kinetics of the ORR is

modelled by using the rate constants of each elementary reaction step in a mean-field differential equation approach. Here we use the 11 elementary reactions we identified during our previous DFT studies. These and their corresponding activation energies, ZPE corrected activation energies and Gibbs free energies (ZPE plus room temperature vibrational enthalpy and entropy correction) are shown in table 1.

Elementary reaction step	$\Delta E^{\ddagger}(\mathrm{kJ/mol})$	$\Delta E^{\ddagger}_{\mathrm{ZPE}}(\mathrm{kJ/mol})$	$\Delta G^{\ddagger}_{298}(\mathrm{kJ/mol})$
$H_2O^* \rightarrow H_2O + *$	55 [10]	55 [10]	55 [10]
$H_2O_2^* \rightarrow H_2O_2 + *$	40	-7	-44
$O_2 + * \rightarrow O_2^*$	0	0	0
$O_2^* \rightarrow O_2 + *$	15 [11]	15 [11]	15 [11]
$H_2 + 2* \rightarrow 2H^*$	0	0	0
$2H^* \rightarrow H_2 + 2*$	72 [12]	72 [12]	72 [12]
$O_2^* + * \rightarrow 2O^*$	63	61	62
$2O^* \rightarrow O_2^* + *$	164	164	182
$O^* + H^* \rightarrow OH^* + *$	142	142	160
$OH^* + * \rightarrow O^* + H^*$	183	167	167
$OH^* + H^* \rightarrow H_2O + *$	45	53	75
$H_2O^* + * \rightarrow OH^* + H^*$	124	109	112
$O_2^* + H^* \rightarrow OOH^* + *$	27	36	67
$OOH^* + * \rightarrow O_2^* + H^*$	62	45	62
$OOH^* + * \rightarrow O^* + OH^*$	72	65	69
$O^* + OH^* \rightarrow OOH^* + *$	178	183	202
$OOH^* + H^* \rightarrow HOOH^* + *$	67	78	102
$HOOH^* + * \rightarrow OOH^* + H^*$	91	74	74
$HOOH^* + * \rightarrow 2OH^*$	45	34	33
$2OH^* \rightarrow HOOH^* + *$	168	181	202

Table 1: Activation energies from previous calculations [2, 3, 9] and external sources used for the microkinetic model.

Using these energies, the rate constants (Transition state theory) for each reaction were calculated. We assume the frequency factors to be equal for all reactions. The rate constant k^i_{ads} for the unimolecular adsorption of O_2 and H_2 from the gas-phase was calculated using the formula

$$k^i_{\mathrm{ads}}(P_i,T) = \frac{A_{\mathrm{site}} P_i \sigma_i}{\sqrt{2\pi m_i k_{\mathrm{B}} T}} \qquad (2)$$

.

Here A_{site} is the area of adsorption site, P_i the partial pressure of component i, σ_i the sticking coefficient of component i, m_i the mass of component i, k_B Boltzmann's constant and T the temperature. The sticking coefficients for the gas-phase components were assumed to be unity. To take also lateral interactions between adsorbed species into account, the adsorption energies from temperature programmed desorption (TPD) measurements were included into the kinetic model [10-12]. However the explicit dependence of activation barriers on lateral interactions are not included into this model. Since the temperature range of our simulations is far above the desorption temperature of H_2O (300 K), its autocatalytic activity is negligible. In contrast to electrochemical ORR where direct reactions with the electrolyte can occur, in gas-phase we consider only LH-type reactions mechanisms.

Finally the rates for each elementary reaction step and the overall rate for per surface atom are obtained by first calculating the steady-state surface coverages and these are calculated by solving the differential equation for the coverage of each species.

To measure the individual influence of a reaction step i on the overall reaction rate R, the *degree of rate control* $X_{RC,i}$ is introduced by:

$$X_{RC,i} = \frac{k_i}{R}\left(\frac{\partial R}{\partial k_i}\right) = \left(\frac{\partial \ln R}{\partial \ln k_i}\right) \qquad (3)$$

.

Here the overall rate R contains the rate constants for all other reaction steps k_j ($j \neq i$). The higher the value of X_i, the greater is the influence of reaction step i on the overall reaction. Positive values increase the overall rate (*rate-controlling* step), negative values decrease the overall rate (*inhibiting* step).

Results

First we show the importance of using Gibbs free energies instead of only ZPE corrected energies or sole activation energies for the kinetic simulations. Figure 2 shows three different kinetic models for the water formation rate constant using one of these energies each for simulations.

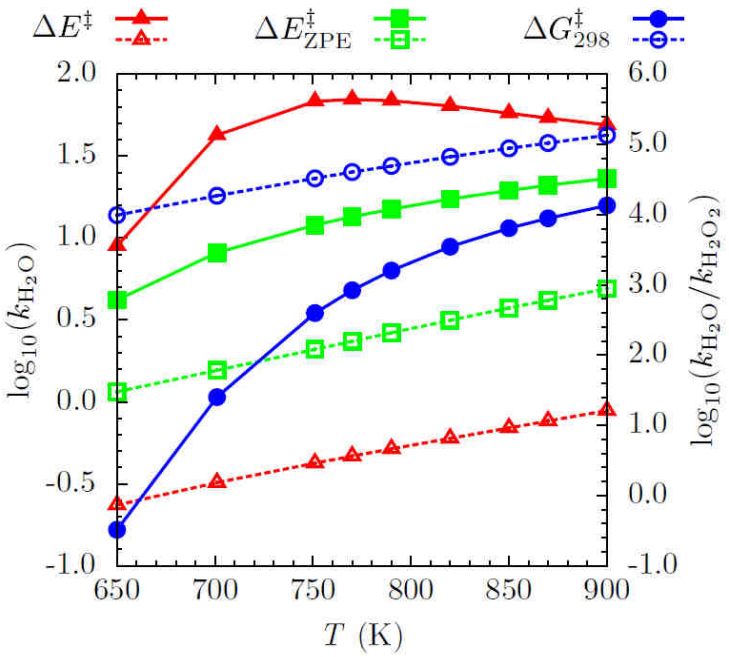

Figure 2: Comparison of the temperature dependence of the rate constant of water formation log k_{H2O} (solid lines) and selectivity log k_{H2O}/k_{H2O2} (dashed lines) for microkinetic models where sole activation energies (red), ZPE corrected energies (green) and Gibbs free energies at room temperature (blue) were used. (Adapted from [13]).

It is evident that the use of different levels of correction for the activation barrier leads to a difference in rate constants and selectivity up to several orders of magnitude. Therefore we use the physically most meaningful Gibbs free energies for further simulations.

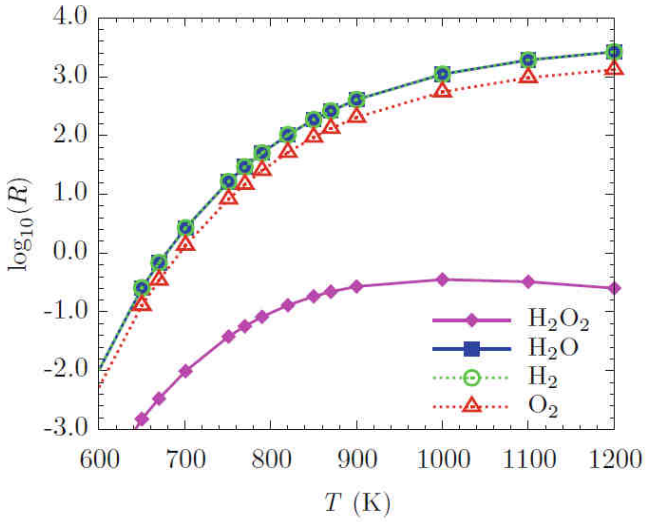

Figure 3: Simulation results showing the reaction rates for the formation of products (solid lines) and the consumption of reactants (dashed lines) for a mixture of O_2 and H_2 with partial pressures of 1/3 and 2/3 atm. (Adapted from [13]).

First the temperature dependence of the rate constants for the formation of H_2O and H_2O_2 was investigated, using a stoichiometric mixture of H_2 and O_2 at a constant total pressure of 1 atm. Figure 3 shows that the rate of water production is several magnitudes higher than the production of H_2O_2 and increases with temperature, whereas the rate of H_2O_2 decreases at high temperatures. Thus the consumption rates of the reactants is mostly determined by the rate of water formation. Although some

simple predictions for the preferred pathways can be made by looking at the barriers alone, a detailed analysis of the reaction maps for each simulation shows that the O_2 and OOH dissociation pathways are clearly preferred over the HOOH dissociation pathway, since $HOOH^*$ is more likely to desorb than to dissociate. Thus O_2^* dissociation is inhibited at low temperatures, the formation of OH^* is here the rate determining step. The negative reaction order of O_2 shown in figure 4a and the surface coverage O^* lead to the conclusion, that a high oxygen coverage prevents hydrogen adsorption and thus lowers the ORR activity.

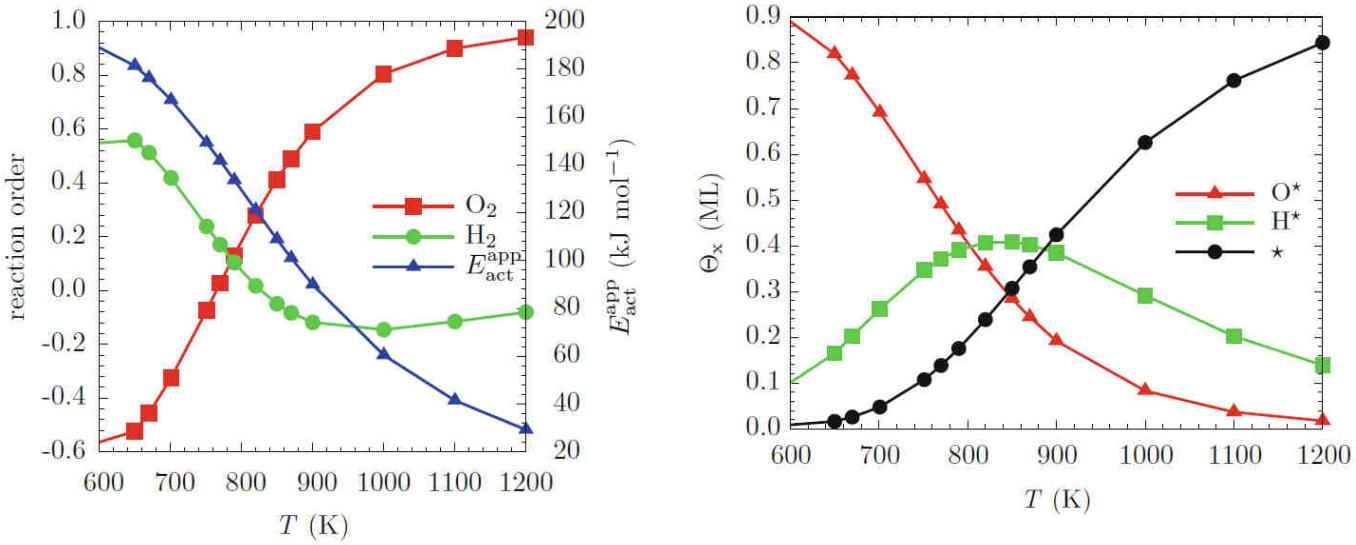

(a) reaction rates (b) surface coverage

Figure 4: Simulation results showing **(a)** the reaction order for the reactants and the apparent activation energy, (b) the surface coverage of the most important species (all other surface species have negligible coverages). (Adapted from [13]).

As the reaction order reaches zero at temperatures above 700 K, the surface starts to expose vacant adsorption sites and the O_2^* dissociation is not rate inhibiting but becomes more rate limiting with increasing temperature, whereas the OH^* formation becomes less rate controlling. At the highest simulation temperature the reaction order for O_2 reaches almost unity and for H_2 approaches zero (from negative). These findings for the reaction order are consistent with the temperature dependent coverage of the surface with oxygen and hydrogen (see figure 4b). By calculating the degree of rate control for each reaction step and temperature (see figure 5), we also identify the O_2^* dissociation and OH^* as the most critical steps for the overall reaction.

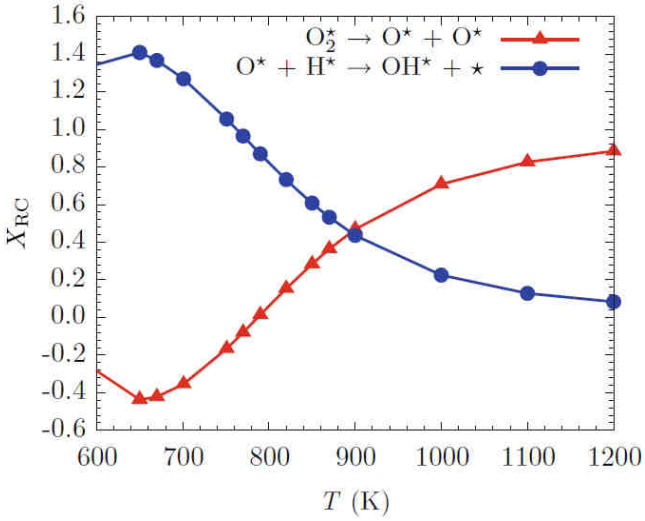

Figure 5: Degree of rate control for the most important reaction steps. The degree of rate control of all other reaction steps is negligible. (Adapted from [13]).

In the next step we investigated the influence of the gas-phase composition (at a fixed pressure of 1 atm) on the rate of water formation. For each temperature we find an optimal ratio $p(O_2)$:$p(H_2)$. An example at 700 K is shown in figure 6a, where the optimal ratio is the stoichiometric one. In addition we see, that the product of the surface concentrations $[H^*]\cdot[O^*]$ correlates to the water formation rate, supporting the hypothesis of OH^* formation being the rate determining step in a temperature range between 600 K and 900 K. A second order polynomial fit yields the computationally exact maximum for each temperature. By plotting the optimal ratio versus temperature and fitting again a second order polynomial, we obtain an empirical function to calculate the best ratio for a given temperature (see figure 6b).

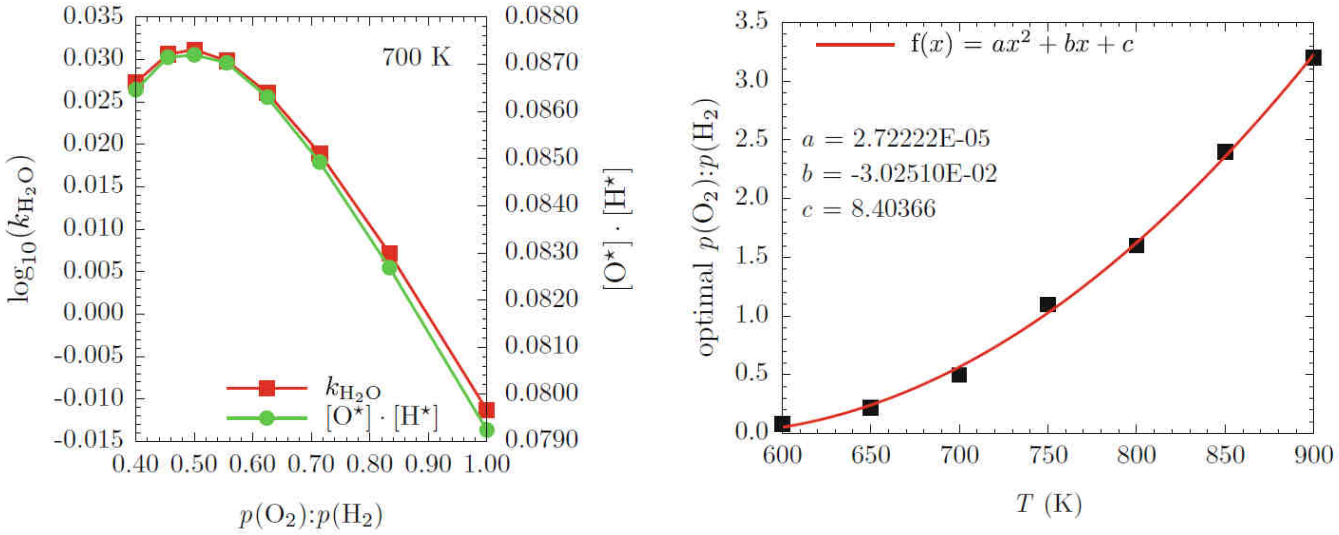

(a) finding the optimal ratio (b) temperature dependence of the optimal ratio

Figure 6: Water formation rate for various reactant ratios in the gas-phase at a total pressure of 1 atm. (Adapted from [13]).

At low temperatures a surplus of hydrogen is needed to yield a higher reaction rate. This is due to the coverage of the surface with O^* (O_2^* dissociation is rate inhibiting) and thus blocking free sites for

hydrogen dissociation. At high temperatures oxygen has mostly desorbed and therefore a higher oxygen partial pressure is needed to drive the reaction (O_2 dissociation is rate controlling). The water formation rates for simulations with various reactant ratios are shown in figure 7.

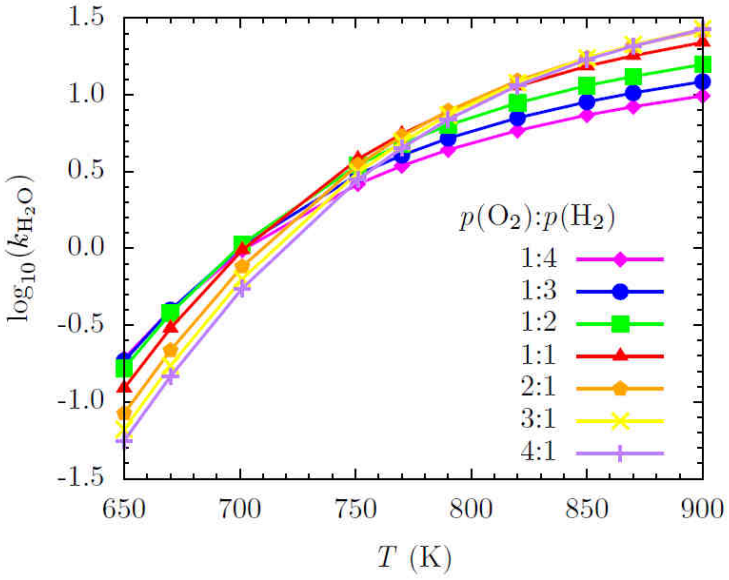

Figure 7: Water formation rates for various reactant ratios in the gas-phase at a total pressure of 1 atm. (Adapted from [13]).

Summary

In the first part of this report the reaction rate constants of the water formation, H_2O_2 formation and the three dissociation pathways (O_2, OOH, HOOH) were calculated, using the potential dependent Gibbs free energies at 0 V and 1.23 V (vs. RHE). Analysing the reaction rates allowed first conclusions on the reaction kinetics. We find that for low potentials (below 0.4 V) the HOOH mechanism is the preferred reaction pathway, however for high potentials (above 0.75 V) the O_2 dissociation mechanism becomes the preferred pathway.

Afterwards we formulated a microkinetic modelling approach for the water formation on Pt. In order to test this approach we first focus on the gas-phase water formation reaction using the elementary reaction steps found by explicit DFT calculations. The highest catalytic activity in this model was found in the temperature range between 600 and 900 K. Further, we found the kinetic model to be very sensitive to the activation barriers as a hint to think carefully about corrections to the sole activation energies obtained from DFT calculations. For a stoichiometric mixture of hydrogen and oxygen we found the OH^* formation to be rate controlling at low temperatures (600 K), whereas at high temperatures (900 K) the O_2^* dissociation becomes the rate controlling reaction step. Furthermore we notice, that below 780 K the O_2^* dissociation is rate inhibiting due to blocking free sites for hydrogen to dissociate. Finally we obtained a temperature dependent relation for the optimal partial pressure ratio of hydrogen and oxygen. These findings are in good agreement with experimental results reported in literature.

After formulating the microkinetic approach and testing it against the well-known gas phase water formation reaction, future studies will now concentrate on full kinetic studies of the electrochemical ORR. The knowledge of all important electrochemical reaction steps and their activation energies should provide ideas to improve the catalyst design by synthesizing materials which lower the relevant activation energies.

References

[1] Jacob, T. (2006), *Fuel Cells*, 6(3–4), 159–181.
[2] Keith, J.A. and Jacob, T. (2010), *Angew. Chem. Int. Ed.*, 49 (49), 9521–9525.
[3] Keith, J.A., Jerkiewicz, G., and Jacob, T. (2010), *ChemPhysChem*, 11 (13), 2779–2794.
[4] Eyring, H. (1935), *J. Chem. Phys.*, 3, 107–115.
[5] Marx, D. (2006), *Chem. Phys. Chem.*, 7, 1848–1870.
[6] Marković, N. M., Gasteiger, H. A., Ross, P. N. (1995), *J. Phys. Chem.*, 99, 3411–3415.
[7] Marković, N., Ross, P., Jr. (1999) in *Interfacial Electrochemistry: Theory, Experiments and Applications* (Ed.: A. Wieckowski), Marcel Dekker, New York, 821–841.
[8] http://www.mkmcxx.nl [12.06.2015]
[9] Muller, J. E., Fantauzzi, D., Jacob, T. (2013), *Multiscale Model Electrochem Syst.*, Wiley, New-York.
[10] Grecea, M. L., Backus, E. H. G., Riedmuller, B., Eichler, A., Kleyn, A. W., Bonn, M. (2004), *J. Phys. Chem. B*, 108(33), 12575.
[11] Gland, J. L. (1980), *Surf. Sci.*, 93(23), 487.
[12] Miller, J. T., Meyers, B. L., Modica, F. S., Lane, G. S., Vaarkamp, M., Konigsberger, D. C. (1993), *J. Catal.*, 143(2), 395.
[13] Fantauzzi, D., Zhu, T., Mueller, J. E., Filot, I. A. W., Hensen, E. J. M., Jacob, T., *Catal. Lett.*, 145, 451–457.